Conformation sequence recovery of a non-periodic object from a diffraction-before-destruction experiment

Chun Hong Yoon,[1,2] Miriam Barthelmess,[3] Richard J. Bean,[1] Flavio Capotondi,[4] Richard A. Kirian,[1] Maya Kiskinova,[4] Emanuele Pedersoli,[4] Lorenzo Raimondi,[4] Francesco Stellato,[1] Fenglin Wang,[1] and Henry N. Chapman[1,5,6,*]

[1]*Center for Free-Electron Laser Science, DESY, Notkestrasse 85, 22607 Hamburg, Germany*
[2]*European XFEL GmbH, Albert Einstein Ring 19, 22761 Hamburg, Germany*
[3]*Photon Science, DESY, Notkestrasse 85, 22607 Hamburg, Germany*
[4]*Fermi, Elettra Sincrotrone Trieste, SS 14 – km 163.5, 34149 Basovizza, Trieste, Italy*
[5]*University of Hamburg, Luruper Chaussee 149, Hamburg, 22761, Germany*
[6]*Centre for Ultrafast Imaging, Luruper Chaussee 149, Hamburg, 22761, Germany*
[*]*henry.chapman@desy.de*

Abstract: Knowledge of the sequence of different conformational states of a protein molecule is key to better understanding its biological function. A diffraction pattern from a single conformational state can be captured with an ultrafast X-ray Free-Electron Laser (XFEL) before the target is completely annihilated by the radiation. In this paper, we report the first experimental demonstration of conformation sequence recovery using diffraction patterns from randomly ordered conformations of a non-periodic object using the dimensional reduction technique Isomap and coherent diffraction imaging.

© 2014 Optical Society of America

OCIS codes: (260.1960) Diffraction theory; (150.0150) Machine vision; (290.5840) Scattering, molecules; (320.7100) Ultrafast measurements.

References and links

1. H. N. Chapman, "X-ray imaging beyond the limits," Nat. Mater. **8**(4), 299–301 (2009).
2. H. N. Chapman, A. Barty, M. J. Bogan, S. Boutet, M. Frank, S. P. Hau-Riege, S. Marchesini, B. W. Woods, S. Bajt, W. H. Benner, R. A. London, E. Plönjes, M. Kuhlmann, R. Treusch, S. Düsterer, T. Tschentscher, J. R. Schneider, E. Spiller, T. Möller, C. Bostedt, M. Hoener, D. A. Shapiro, K. O. Hodgson, D. van der Spoel, F. Burmeister, M. Bergh, C. Caleman, G. Huldt, M. M. Seibert, F. R. N. C. Maia, R. W. Lee, A. Szöke, N. Timneanu, and J. Hajdu, "Femtosecond diffractive imaging with a soft-X-ray free-electron laser," Nat. Phys. **2**(12), 839–843 (2006).
3. R. Neutze, R. Wouts, D. van der Spoel, E. Weckert, and J. Hajdu, "Potential for biomolecular imaging with femtosecond X-ray pulses," Nature **406**(6797), 752–757 (2000).
4. B. Ziaja and N. Medvedev, "Modelling ultrafast transitions within laser-irradiated solids," High Energy Density Phys. **8**(1), 18–29 (2012).
5. M. M. Seibert, T. Ekeberg, F. R. N. C. Maia, M. Svenda, J. Andreasson, O. Jönsson, D. Odić, B. Iwan, A. Rocker, D. Westphal, M. Hantke, D. P. DePonte, A. Barty, J. Schulz, L. Gumprecht, N. Coppola, A. Aquila, M. Liang, T. A. White, A. Martin, C. Caleman, S. Stern, C. Abergel, V. Seltzer, J. M. Claverie, C. Bostedt, J. D. Bozek, S. Boutet, A. A. Miahnahri, M. Messerschmidt, J. Krzywinski, G. Williams, K. O. Hodgson, M. J. Bogan, C. Y. Hampton, R. G. Sierra, D. Starodub, I. Andersson, S. Bajt, M. Barthelmess, J. C. H. Spence, P. Fromme, U. Weierstall, R. Kirian, M. Hunter, R. B. Doak, S. Marchesini, S. P. Hau-Riege, M. Frank, R. L. Shoeman, L. Lomb, S. W. Epp, R. Hartmann, D. Rolles, A. Rudenko, C. Schmidt, L. Foucar, N. Kimmel, P. Holl, B. Rudek, B. Erk, A. Hömke, C. Reich, D. Pietschner, G. Weidenspointner, L. Strüder, G. Hauser, H. Gorke, J. Ullrich, I. Schlichting, S. Herrmann, G. Schaller, F. Schopper, H. Soltau, K. U. Kühnel, R. Andritschke, C. D. Schröter, F. Krasniqi, M. Bott, S. Schorb, D. Rupp, M. Adolph, T. Gorkhover, H. Hirsemann, G. Potdevin, H. Graafsma, B. Nilsson, H. N. Chapman, and J. Hajdu, "Single mimivirus particles intercepted and imaged with an X-ray laser," Nature **470**(7332), 78–81 (2011).
6. M. J. Bogan, D. Starodub, C. Y. Hampton, and R. G. Sierra, "Single-particle coherent diffractive imaging with a soft x-ray free electron laser: towards soot aerosol morphology," J. Phys. At. Mol. Opt. Phys. **43**(19), 194013 (2010).
7. A. P. Mancuso, T. Gorniak, F. Staier, O. M. Yefanov, R. Barth, C. Christophis, B. Reime, J. Gulden, A. Singer, M. E. Pettit, T. Nisius, T. Wilhein, C. Gutt, G. Grübel, N. Guerassimova, R. Treusch, J. Feldhaus, S. Eisebitt, E.

Weckert, M. Grunze, A. Rosenhahn, and I. A. Vartanyants, "Coherent imaging of biological samples with femtosecond pulses at the free-electron laser FLASH," New J. Phys. **12**(3), 035003 (2010).

8. L. Redecke, K. Nass, D. P. DePonte, T. A. White, D. Rehders, A. Barty, F. Stellato, M. Liang, T. R. M. Barends, S. Boutet, G. J. Williams, M. Messerschmidt, M. M. Seibert, A. Aquila, D. Arnlund, S. Bajt, T. Barth, M. J. Bogan, C. Caleman, T. C. Chao, R. B. Doak, H. Fleckenstein, M. Frank, R. Fromme, L. Galli, I. Grotjohann, M. S. Hunter, L. C. Johansson, S. Kassemeyer, G. Katona, R. A. Kirian, R. Koopmann, C. Kupitz, L. Lomb, A. V. Martin, S. Mogk, R. Neutze, R. L. Shoeman, J. Steinbrener, N. Timneanu, D. Wang, U. Weierstall, N. A. Zatsepin, J. C. H. Spence, P. Fromme, I. Schlichting, M. Duszenko, C. Betzel, and H. N. Chapman, "Natively inhibited Trypanosoma brucei Cathepsin B structure determined by using an X-ray laser," Science **339**(6116), 227–230 (2013).

9. S. Boutet, L. Lomb, G. J. Williams, T. R. M. Barends, A. Aquila, R. B. Doak, U. Weierstall, D. P. DePonte, J. Steinbrener, R. L. Shoeman, M. Messerschmidt, A. Barty, T. A. White, S. Kassemeyer, R. A. Kirian, M. M. Seibert, P. A. Montanez, C. Kenney, R. Herbst, P. Hart, J. Pines, G. Haller, S. M. Gruner, H. T. Philipp, M. W. Tate, M. Hromalik, L. J. Koerner, N. van Bakel, J. Morse, W. Ghonsalves, D. Arnlund, M. J. Bogan, C. Caleman, R. Fromme, C. Y. Hampton, M. S. Hunter, L. C. Johansson, G. Katona, C. Kupitz, M. Liang, A. V. Martin, K. Nass, L. Redecke, F. Stellato, N. Timneanu, D. Wang, N. A. Zatsepin, D. Schafer, J. Defever, R. Neutze, P. Fromme, J. C. H. Spence, H. N. Chapman, and I. Schlichting, "High-resolution protein structure determination by serial femtosecond crystallography," Science **337**(6092), 362–364 (2012).

10. J. Kern, R. Alonso-Mori, R. Tran, J. Hattne, R. J. Gildea, N. Echols, C. Glöckner, J. Hellmich, H. Laksmono, R. G. Sierra, B. Lassalle-Kaiser, S. Koroidov, A. Lampe, G. Han, S. Gul, D. Difiore, D. Milathianaki, A. R. Fry, A. Miahnahri, D. W. Schafer, M. Messerschmidt, M. M. Seibert, J. E. Koglin, D. Sokaras, T. C. Weng, J. Sellberg, M. J. Latimer, R. W. Grosse-Kunstleve, P. H. Zwart, W. E. White, P. Glatzel, P. D. Adams, M. J. Bogan, G. J. Williams, S. Boutet, J. Messinger, A. Zouni, N. K. Sauter, V. K. Yachandra, U. Bergmann, and J. Yano, "Simultaneous femtosecond X-ray spectroscopy and diffraction of photosystem II at room temperature," Science **340**(6131), 491–495 (2013).

11. P. A. Penczek, M. Kimmel, and C. M. T. Spahn, "Identifying conformational states of macromolecules by eigen-analysis of resampled cryo-EM images," Structure **19**(11), 1582–1590 (2011).

12. S. H. W. Scheres, H. Gao, M. Valle, G. T. Herman, P. P. B. Eggermont, J. Frank, and J. M. Carazo, "Disentangling conformational states of macromolecules in 3D-EM through likelihood optimization," Nat. Methods **4**(1), 27–29 (2007).

13. P. Schwander, R. Fung, G. N. Phillips, Jr., and A. Ourmazd, "Mapping the conformations of biological assemblies," New J. Phys. **12**(3), 035007 (2010).

14. P. Schwander, D. Giannakis, C. H. Yoon, and A. Ourmazd, "The symmetries of image formation by scattering. II. Applications," Opt. Express **20**(12), 12827–12849 (2012).

15. C. H. Yoon, P. Schwander, C. Abergel, I. Andersson, J. Andreasson, A. Aquila, S. Bajt, M. Barthelmess, A. Barty, M. J. Bogan, C. Bostedt, J. Bozek, H. N. Chapman, J. M. Claverie, N. Coppola, D. P. DePonte, T. Ekeberg, S. W. Epp, B. Erk, H. Fleckenstein, L. Foucar, H. Graafsma, L. Gumprecht, J. Hajdu, C. Y. Hampton, A. Hartmann, E. Hartmann, R. Hartmann, G. Hauser, H. Hirsemann, P. Holl, S. Kassemeyer, N. Kimmel, M. Kiskinova, M. Liang, N. T. D. Loh, L. Lomb, F. R. N. C. Maia, A. V. Martin, K. Nass, E. Pedersoli, C. Reich, D. Rolles, B. Rudek, A. Rudenko, I. Schlichting, J. Schulz, M. Seibert, V. Seltzer, R. L. Shoeman, R. G. Sierra, H. Soltau, D. Starodub, J. Steinbrener, G. Stier, L. Strüder, M. Svenda, J. Ullrich, G. Weidenspointner, T. A. White, C. Wunderer, and A. Ourmazd, "Unsupervised classification of single-particle X-ray diffraction snapshots by spectral clustering," Opt. Express **19**(17), 16542–16549 (2011).

16. J. B. Tenenbaum, V. de Silva, and J. C. Langford, "A global geometric framework for nonlinear dimensionality reduction," Science **290**(5500), 2319–2323 (2000).

17. E. Allaria, R. Appio, L. Badano, W. A. Barletta, S. Bassanese, S. G. Biedron, A. Borga, E. Busetto, D. Castronovo, P. Cinquegrana, S. Cleva, D. Cocco, M. Cornacchia, P. Craievich, I. Cudin, G. D'Auria, M. Dal Forno, M. B. Danailov, R. De Monte, G. De Ninno, P. Delgiusto, A. Demidovich, S. Di Mitri, B. Diviacco, A. Fabris, R. Fabris, W. Fawley, M. Ferianis, E. Ferrari, S. Ferry, L. Froehlich, P. Furlan, G. Gaio, F. Gelmetti, L. Giannessi, M. Giannini, R. Gobessi, R. Ivanov, E. Karantzoulis, M. Lonza, A. Lutman, B. Mahieu, M. Milloch, S. V. Milton, M. Musardo, I. Nikolov, S. Noe, F. Parmigiani, G. Penco, M. Petronio, L. Pivetta, M. Predonzani, F. Rossi, L. Rumiz, A. Salom, C. Scafuri, C. Serpico, P. Sigalotti, S. Spampinati, C. Spezzani, M. Svandrlik, C. Svetina, S. Tazzari, M. Trovo, R. Umer, A. Vascotto, M. Veronese, R. Visintini, M. Zaccaria, D. Zangrando, and M. Zangrando, "Highly coherent and stable pulses from the FERMI seeded free-electron laser in the extreme ultraviolet," Nat. Photonics **6**(10), 699–704 (2012).

18. F. Capotondi, E. Pedersoli, N. Mahne, R. H. Menk, G. Passos, L. Raimondi, C. Svetina, G. Sandrin, M. Zangrando, M. Kiskinova, S. Bajt, M. Barthelmess, H. Fleckenstein, H. N. Chapman, J. Schulz, J. Bach, R. Frömter, S. Schleitzer, L. Müller, C. Gutt, and G. Grübel, "Invited article: Coherent imaging using seeded free-electron laser pulses with variable polarization: First results and research opportunities," Rev. Sci. Instrum. **84**(5), 051301 (2013).

19. en.wikipedia.org/wiki/File:Muybridge_race_horse_animated.gif.

20. I. McNulty, J. Kirz, C. Jacobsen, E. H. Anderson, M. R. Howells, and D. P. Kern, "High-resolution imaging by Fourier transform X-ray holography," Science **256**(5059), 1009–1012 (1992).

21. N. Davidson, "NADIA Software Project Page," http://cxscode.ph.unimelb.edu.au/.

22. J. R. Fienup, "Phase retrieval algorithms: a comparison," Appl. Opt. **21**(15), 2758–2769 (1982).

23. S. Marchesini, H. He, H. N. Chapman, S. P. Hau-Riege, A. Noy, M. R. Howells, U. Weierstall, and J. C. H. Spence, "X-ray image reconstruction from a diffraction pattern alone," Phys. Rev. B **68**(14), 140101 (2003).

24. H. N. Chapman, A. Barty, S. Marchesini, A. Noy, S. P. Hau-Riege, C. Cui, M. R. Howells, R. Rosen, H. He, J. C. H. Spence, U. Weierstall, T. Beetz, C. Jacobsen, and D. Shapiro, "High-resolution ab initio three-dimensional x-ray diffraction microscopy," J. Opt. Soc. Am. A **23**(5), 1179 (2006).
25. K. V. Mardia, J. T. Kent, and J. M. Bibby, *Multivariate Analysis* (Academic, 1979).

1. Introduction

A diffraction pattern from a non-periodic object such as a large macromolecule or a virus may be captured by an ultrafast X-ray Free-Electron Laser (XFEL) before the target is completely annihilated by the radiation. This so called "Diffraction-before-destruction" technique [1,2] requires coherent X-ray pulses with higher peak brilliance than modern synchrotron sources can produce. Extremely brief pulses of femtosecond duration are required in order to outrun the radiation damage processes that occur within a few tens of femtoseconds, depending on the spatial resolution [3,4]. Femtosecond diffractive imaging from a non-periodic object was first demonstrated using a soft X-ray Free-Electron Laser (XFEL) in 2006 [2]. The emergence of hard XFELs has enabled structural studies of nano-structured single particles [5–7] and microcrystals [8,9]. Recently, a pump-probe experiment at LCLS showed it may be possible to probe the conformational states of the structure of Photosystem II microcrystals [10] at particular times after exposure to an optical pulse.

Here we utilize Isomap, a manifold embedding algorithm, to recover the motion sequence of an object from a series of diffraction patterns in random unknown order. This matches the case of single particle experiments in which individual particles are delivered to the x-ray beam one at a time. Conformation recovery is an active area of research in other single-particle imaging techniques [11,12].

Manifold-embedding algorithms have been shown to be effective at recovering structure and conformational states from simulated diffraction patterns [13,14] and have been used to sort diffraction patterns of viruses and nanoparticles recorded at LCLS [15]. In this paper, we report the experimental demonstration of conformation sequence recovery using diffraction patterns from random instances of single micro-fabricated objects illuminated by soft X-ray FEL pulses. The basic approach is to use dimensional reduction to capture the underlying parameter of change (i.e., the motion sequence) of the particle using Isomap [16]. As this is the first attempt at such a recovery using femtosecond FEL pulses, it seems fitting to reconstruct the sequence of the first motion picture in history, the "horse in motion" by Eadweard Muybridge. The series of frames used for the experiment, shown in in Fig. 1, is based on the original Muybridge series.
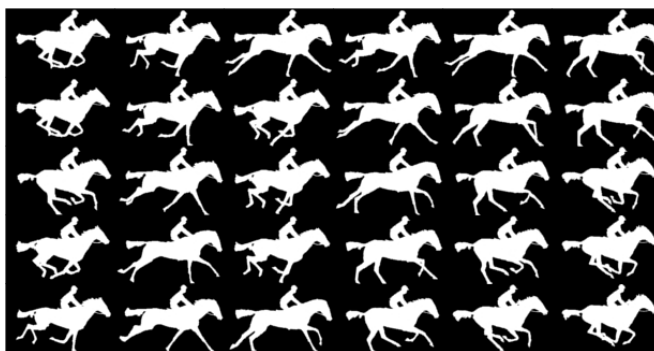

Fig. 1. Images of a galloping horse in random order. Thirty frames sample the full period of motion.

2. Experimental setup

Measurements were carried out at the coherent diffraction imaging (CDI) experimental station at the DiProI beamline at FERMI@Elettra FEL. Compared to SASE FELs, the seeded FERMI FEL X-ray pulses have much higher spectral purity and stability, an asset for single-shot experiments [17]. The experimental station can host all necessary components and

diagnostics for beam cleaning, reproducible sample alignment and detection systems for collecting diffraction patterns from fixed or injected samples in a single shot or an integrative non-destructive mode. The FEL beam, focused with a Kirkpatrick-Baez (K-B) mirror system, enters the chamber through a circular aperture. The number of pulses the sample is exposed to is controlled by a fast shutter. The beamline is equipped with a gas cell and Al filters which can be used to attenuate the FEL pulse intensity in a controllable manner by up to four orders of magnitude. A detailed description of the beamline and the measurement station can be found in ref [18]. The present study was carried out at a wavelength of 32.5 nm with a pulse energy of ~30 μJ. The flux in the 25×25 μm^2 focal spot onto the sample was 8.6×10^{21} ph/μm^2. Diffraction patterns were collected using a detection system in an indirect configuration where the scattered light is reflected onto a CCD (Princeton Instrument MTE2048B) by a multilayer mirror with a central hole to allow the passage of the undiffracted beam. For each exposure all relevant parameters (intensity, spectrum of the incoming radiation and diffraction pattern) are acquired in synchronized mode.

Frames from the animated "horse in motion" [19] were first converted to binary images, retaining information only from the horse and rider, and intermediate frames were added manually using an image manipulation program to produce a periodic 30 frame sequence of a galloping horse (Fig. 1). These images were then deposited in Platinum onto 100 μm × 100 μm, 30 nm thick Si$_3$N$_4$ windows on a Si wafer by Focused Ion Beam (FIB) (Fig. 2(a)). Pt was deposited via a gas injection system (C$_5$H$_4$CH$_3$Pt(CH$_3$)$_3$) with the electron beam at 43 pA at 5 keV. The horse dimensions were approximately 5×7 μm^2 and 20 nm thickness (Pt content of approximately 16%). Some membranes were contaminated by an unknown substance which also diffracted strongly such that holographic images of the horse can sometimes be seen in the Patterson function (autocorrelation) of the diffracted intensities (Fig. 2(b)) [20].
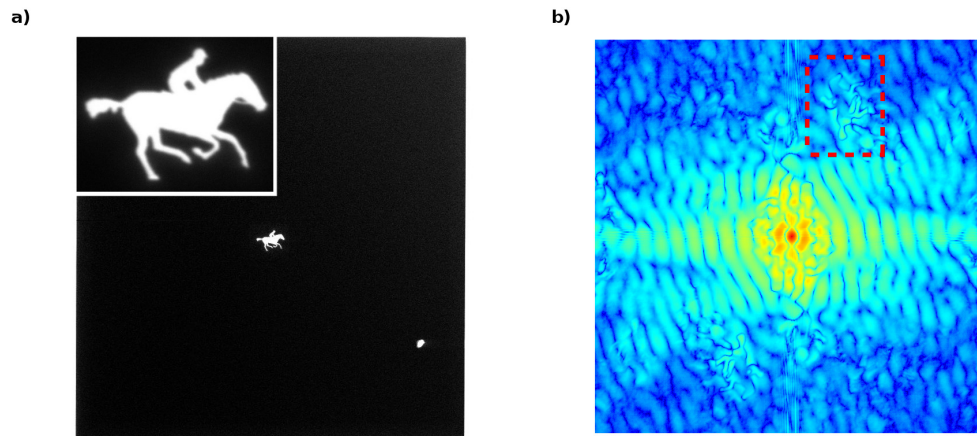
a)   b)

Fig. 2. Sample fabrication using a focused ion beam. a) Electron micrograph of a Pt deposited horse on a silicon nitride membrane (100 μm × 100 μm). A magnified view of the horse is shown in the inset. Some membranes were contaminated by an unknown substance (as can be seen here on the lower right corner of the membrane) which also diffracted. (b) Holographic images of the horse (dashed lines) can sometimes be seen from the Patterson function (direct Fourier transform) of the diffracted intensities.

The windows were placed into the beam focus in random frame order. Diffraction patterns were collected using 100-femtosecond pulses at full FEL transmission (Fig. 3). The wavelength spectrum is also displayed in Fig. 3 which shows that the pulses are monochromatic with varying intensities. The extremes of the wavelength spectrum are shown in Figs. 3(b) and 3(c). The intensity variation between diffraction patterns is primarily due to the change in incident intensity from the FEL and also the positioning of the sample relative to the centre of the Si$_3$N$_4$ window.
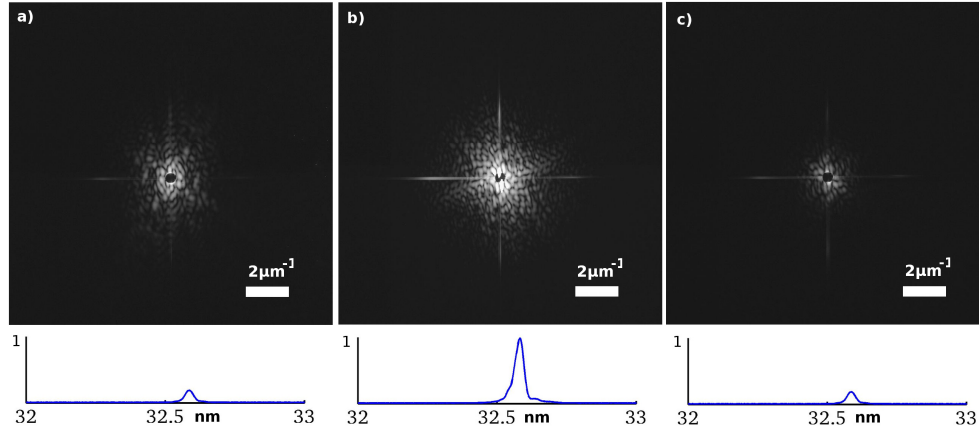
Fig. 3. (a)-(c) Diffraction patterns collected at FERMI. Frames 1, 23 and 26 are shown in log scale (left to right). The scale bar represents the exchanged momentum of 2 μm-1. Central orthogonal streaks are caused by beam interaction with the square Si window frame. Incoming wavelength spectrum centred around 32.5 nm is also shown below each diffraction pattern in linear scale (arbitrary units). A wide range of shot-to-shot pulse intensities can be seen.

Diffraction-before-destruction imaging is demonstrated in Fig. 4. Top panels (a) and (b) show the measured single-shot diffraction pattern and the averaged reconstructed horse. We used 6000 iterations of the Hybrid Input-Output (HIO) algorithm [21] followed by 100 iterations of the Error Reduction (ER) algorithm starting with a loose rectangular support and applying the shrinkwrap algorithm [22] every 100 iterations. Reconstructions were carried out with the CXS software suite [23]. Reconstruction resolution is estimated by the phase retrieval transfer function (PRTF) [24] defined as

$$PRTF(u) = \frac{\left| \left\langle \Gamma(u) \exp(i\Phi_0) \right\rangle \right|}{\sqrt{I(u)}}, \tag{1}$$

where Γ is the diffraction amplitude with retrieved phases and $\langle \ \rangle$ denotes an ensemble average over independent reconstructions. Using 21 out of 25 converged reconstructions, the PRTF is calculated using 0.1 subpixel alignment and the resulting maximum exchange momentum at cutoff $1/e$ is 3.3 μm^{-1} or estimated half period resolution of 0.15 μm (see Fig. 4(c)). The single-shot image in Fig. 4(d) collected with a second FEL pulse confirms that the horse has been annihilated, i.e. the sample is destroyed with the first FEL pulse.
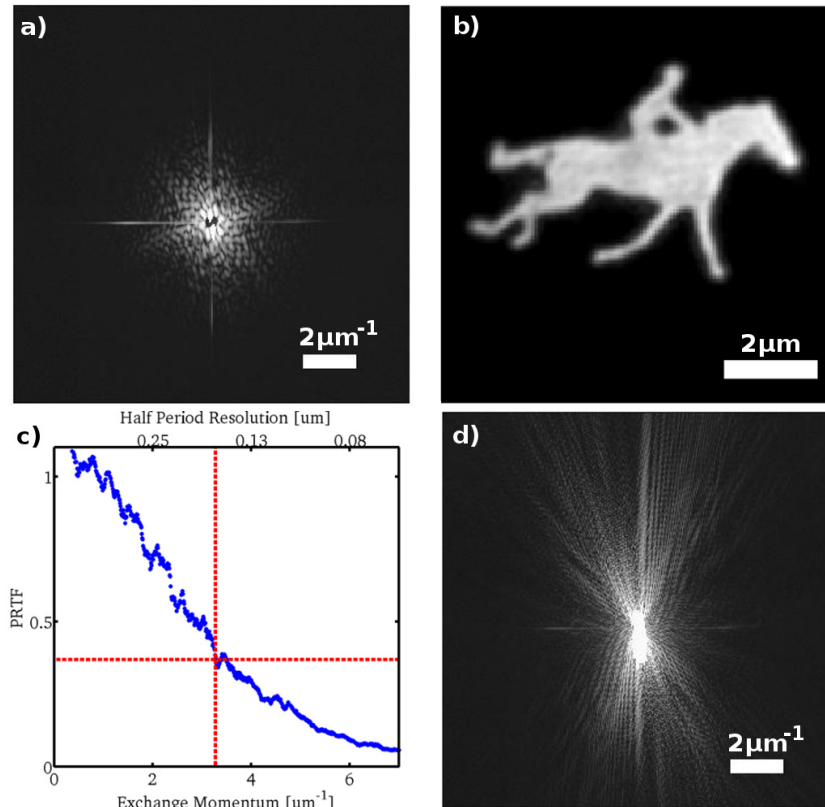
Fig. 4. Demonstration of diffraction-before-destruction: (a) Diffraction pattern from frame 26 in log scale. The scale bar represents the exchanged momentum of 2 μm-1. (c) Phase retrieval transfer function estimates the half period resolution to be 0.15 μm. (d) Diffraction signal collected after the initial X-ray pulse confirms that the sample is destroyed.

3. Dimensional reduction using Isomap

Isomap [16] is a dimension reduction technique used to discover underlying non-linear degrees of freedom in a high-dimensional topological data set while preserving its connectivity. In classical linear dimension reduction techniques such as principal component analysis (PCA) and multidimensional scaling (MDS) [25], one finds a low dimensional embedding that best preserves the variance of the data set or the pair-wise distances, respectively. Isomap is an extension of MDS where geodesic distances (as opposed to pair-wise Euclidean distances) are preserved on a weighted graph. The use of geodesic distances is based on the observation that a Euclidean distance is only a good measure of local similarity and is unreliable for a pair of data points that are far apart on a curved manifold. The algorithm has a single input parameter, k-nearest-neighbours (KNN), which is used for building up the weighted graph G. The similarity metric that determines the weight w between two nodes i and j is data dependent and chosen to be positive ($w_{ij} > 0$) and symmetric ($w_{ji} = w_{ij}$). Isomap estimates the geodesic distances between all data points by calculating the shortest path distances on the weighted graph G, then applies MDS to the graph distances which best preserves the geodesic distances in a low dimensional space.
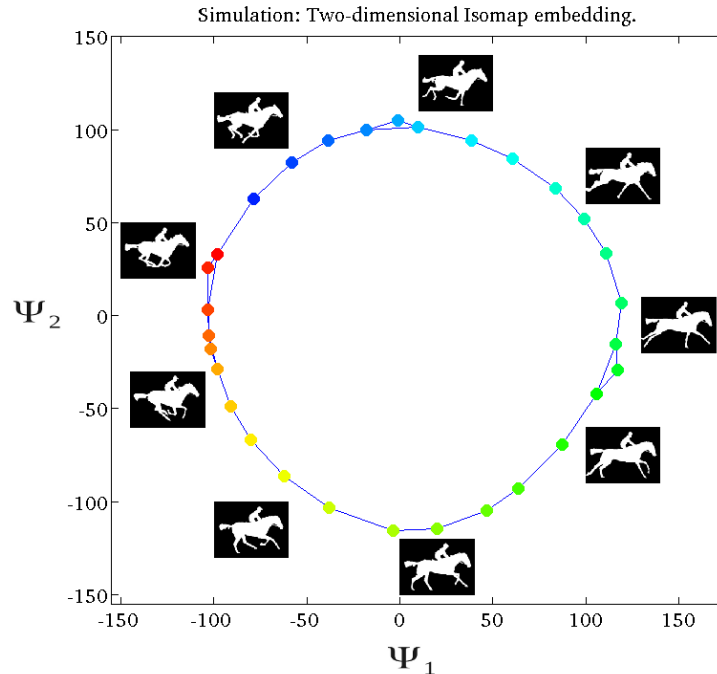
Fig. 5. Simulated recovery of horse in motion using dimensionality reduction with neighbourhood graph. The input consists of 30 diffraction patterns in 202,500 vector space (450 × 450 pixels) of the horse in motion. The first two eigenvectors capture the periodic nature of the motion. The correct frame sequence is shown in colour from red to blue. The connecting lines represent the nearest neighbours. Horse frames are shown next to their corresponding data points.

4. Results

To ensure that we have at least one good pattern for each motion we measured a total of around 110 snapshots (approximately 4 copies of each conformation). Highly saturated diffraction patterns were more difficult to preprocess and consequently weak diffraction patterns were selected for conformation sequence recovery. In order to apply the Isomap algorithm to recover the correct frame sequence, the 30 raw diffraction patterns (2048 × 2048 pixels) were randomly ordered then preprocessed using the following protocol: 1) detector bias was removed by subtracting X–ray-free background frames, 2) regions of the detector with different responses were corrected using common mode subtraction, 3) high-angle-diffraction regions with low signal were removed by cropping the central region to 450 × 450 pixels, corresponding to a q-cutoff of 2 μm^{-1}, 4) regions behind the beamstop, saturated pixels and orthogonal streaks from the sample windows masked, and 5) image variance was normalized using the formula $X = (Y - \mu)/\sigma$, where Y is the masked diffraction pattern, μ and σ are the mean and standard deviation of Y, and X is the normalized pattern. The similarity metric was taken as the L^2-norm, i.e., $w_{ij} = \left\| X_i - X_j \right\|_2$. Geodesic distances using KNN = 2 were used for manifold embedding using Isomap.

The experiment was also simulated under noiseless conditions in order to demonstrate an ideal embedding. The diffraction patterns were calculated by Fourier transform of the frames in Fig. 1 after zeropadding to match the size of the Si window (2048 × 2048 pixels). High-angle-diffraction regions were removed by cropping the central region to 450 × 450 pixels. The simulated diffraction patterns were then variance normalized.

In the case of simulated manifold embedding, the resulting 2D scatter plot of the first two eigenvectors (ψ_1, ψ_2) reveals a circular manifold (Fig. 5) as expected from embedding a periodic motion. The conformation sequence can be retrieved by ordering the rotational angle of each frame about the origin, i.e., $\arctan(\psi_2/\psi_1)$. The colours from red to blue represent the actual frame numbers (from 1 to 30) which matches the ordering discovered by the manifold. The blue lines represent two nearest neighbour connections.

Embedding results from the experimental data are shown in Fig. 6. Reconstructions are shown next to their corresponding data points and clearly correspond to the motion of the horse. Some errors are evident which deviate from the circular manifold. The experimental errors introduce noise in the L^2-norm similarity metric which can disrupt the correct determination of nearest neighbours. It should be noted that the algorithm would perform better with a finer sampling of motion, since it is sensitive to relative changes between successive frames. The correct sequence on the manifold in Fig. 6 is clockwise, whereas anticlockwise in Fig. 5. The arrow of time cannot be determined from the embedded coordinates alone and must be determined from observing the sequence of reconstructed frames on the manifold. The reconstructed movie can be seen in Fig. 6 (Media 1) with a 2 μm scale bar.
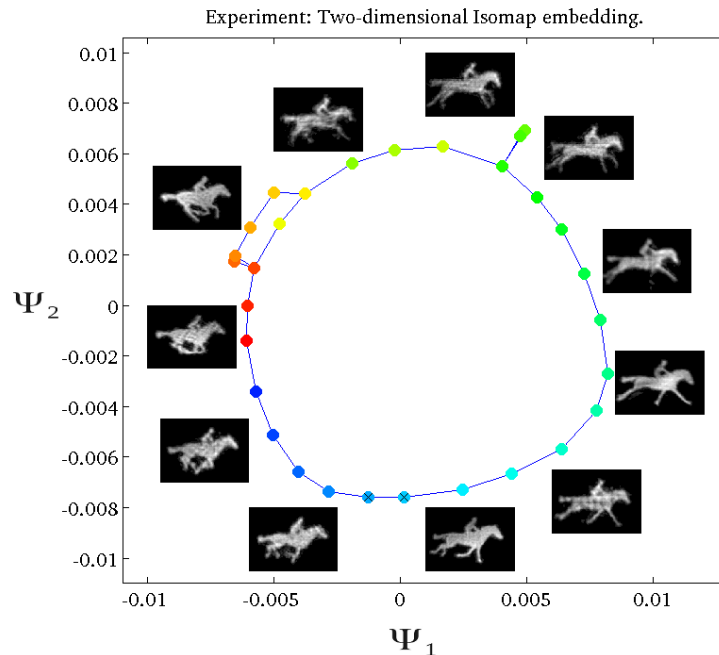

Fig. 6. Recovery of horse in motion using dimensionality reduction with neighbourhood graph. The input consists of 30 diffraction patterns in 202,500 vector space (450 × 450 pixels) of the horse in motion. The first two eigenvectors capture the periodic nature of the motion. The correct frame sequence is shown in colour from red to blue. The connecting lines represent the nearest neighbours. Reconstructions are shown next to their corresponding data points (Media 1).

The two frames that could not be phased after 25 independent attempts (marked as x in Fig. 6) are correctly placed on the manifold. Closer inspection shows that these diffraction patterns correspond to very weak intensities that did not scatter to high q, resulting in low single-to-noise ratio. This suggests that sequencing the frames requires less information than phase retrieval and the algorithm can work in the presence of experimental errors such as detector noise, beam intensity fluctuation and sample membrane contamination.

5. Conclusions

We have experimentally demonstrated the conformation sequence recovery of a non-periodic object from randomized single-shot diffraction patterns. A particularly novel feature of this algorithm is that the conformation sequence can be recovered in Fourier space without resorting to phase retrieval which can be time consuming and/or may not be possible for weakly scattering objects. The algorithm also works in cases where extended areas of the detector are missing or compromised, which is the case for many FEL detector geometries. This algorithm could be applied to single-molecule experiments using molecular alignment via optical lasers. Further theoretical and experimental developments will be needed to recover a set of conformations from randomly oriented biological samples.